



Article

Investigating the Impact of *Xylella Fastidiosa* on Olive Trees by the Analysis of MODIS Terra Satellite Evapotranspiration Time Series by Using the Fisher Information Measure and the Shannon Entropy: A Case Study in Southern Italy

Luciano Telesca ^{1,*}, Nicodemo Abate ², Michele Lovallo ³ and Rosa Lasaponara ¹

¹ Institute of Methodologies for Environmental Analysis, National Research Council, 85050 Tito, Italy; rosa.lasaponara@cnr.it

² Institute of Heritage Science, National Research Council, 85050 Tito, Italy; nicodemoabate@cnr.it

³ Agenzia Regionale per la Protezione dell'Ambiente della Basilicata, 85100 Potenza, Italy; michele.lovallo@arpab.it

* Correspondence: luciano.telesca@cnr.it

Abstract: *Xylella Fastidiosa* has been recently detected for the first time in southern Italy, representing a very dangerous phyto-bacterium capable of inducing severe diseases in many plants. In particular, the disease induced in olive trees is called olive quick decline syndrome (OQDS), which provokes the rapid desiccation and, ultimately, death of the infected plants. In this paper, we analyse about two thousands pixels of MODIS satellite evapotranspiration time series, covering infected and uninfected olive groves in southern Italy. Our aim is the identification of *Xylella Fastidiosa*-linked patterns in the statistical features of evapotranspiration data. The adopted methodology is the well-known Fisher–Shannon analysis that allows one to characterize the time dynamics of complex time series by means of two informational quantities, the Fisher information measure (FIM) and the Shannon entropy power (SEP). On average, the evapotranspiration of *Xylella Fastidiosa*-infected sites is characterized by a larger SEP and lower FIM compared to uninfected sites. The analysis of the receiver operating characteristic curve suggests that SEP and FIM can be considered binary classifiers with good discrimination performance that, moreover, improves if the yearly cycle, very likely linked with the meteo-climatic variability of the investigated areas, is removed from the data. Furthermore, it indicated that FIM exhibits superior effectiveness compared to SEP in discerning healthy and infected pixels.

Keywords: MODIS; satellite; evapotranspiration; Fisher–Shannon; vegetation



Citation: Telesca, L.; Abate, N.; Lovallo, M.; Lasaponara, R. Investigating the Impact of *Xylella Fastidiosa* on Olive Trees by the Analysis of MODIS Terra Satellite Evapotranspiration Time Series by Using the Fisher Information Measure and the Shannon Entropy: A Case Study in Southern Italy. *Remote Sens.* **2024**, *16*, 1242. <https://doi.org/10.3390/rs16071242>

Academic Editors: Pamela L. Nagler, Yaoming Ma, Tanya Doody and Sicong Gao

Received: 11 December 2023

Revised: 12 March 2024

Accepted: 29 March 2024

Published: 31 March 2024



Copyright: © 2024 by the authors. Licensee MDPI, Basel, Switzerland. This article is an open access article distributed under the terms and conditions of the Creative Commons Attribution (CC BY) license (<https://creativecommons.org/licenses/by/4.0/>).

1. Introduction

The rapid evolution of climate change over time and the intensification of global interconnections are catalysts for the onset of biological invasions [1,2], fostering the establishment of highly hazardous phytopathogens, as exemplified by *Xylella Fastidiosa* [3]. The transmission of this bacterium involves various vectors, such as the sap-sucking leafhopper *Homalodisca vitripennis*, native to the southeastern United States and northeastern Mexico [4]. *Xylella Fastidiosa* adversely impacts plants, leading to diverse infections, including Pierce's disease in grapevines [5], olive quick decline [6], bacterial leaf scorch [7], and phony peach disease [8], resulting in significant economic losses in agriculture.

In 2013, *Xylella Fastidiosa* was initially detected in the Salento Peninsula (Apulia) in southeastern Italy, where it rapidly devastated *Olea Europaea* [9], and subsequently, it spread to several other European countries (France, Spain, Portugal, Germany, and Switzerland), posing a genuine phytosanitary emergency [10]. *Xylella Fastidiosa* has been listed as a quarantine organism in many countries across the globe, but the risk level of its establishment mainly in the Mediterranean basin remains very high due to the unintentional transport of insect vectors

(through equipment as a commodity contaminant or vehicle “hitchhiker”) or movement of infected asymptomatic plants or through unknown hosts. Since *Xylella Fastidiosa* is one of the greatest threats to agricultural production not only in Europe but in many countries across the globe, there is an urgent need to devise ad hoc analyses and monitoring.

The initial investigation into *Xylella Fastidiosa* was conducted by Krugner et al. [11], who identified *Xylella Fastidiosa* subsp. *multiplies* in olive trees exhibiting leaf scorch and branch dieback. However, their laboratory experiments failed to replicate the same symptoms observed in field-infected olive trees. Following the detection of *Xylella Fastidiosa* in olive groves in southeastern Italy, a comprehensive study on the bacterium was undertaken in Argentina and Brazil. In these regions, symptomatic olive trees were found to harbor *Xylella Fastidiosa* subsp. *pauca* [12,13], the same subspecies identified in Italian olive trees [14].

Strona et al. [15] discovered that the extensive distribution of olive groves in Apulia (southeastern Italy) and the abundance of *Philaenus spumarius* L., the vector of this bacterium, may have facilitated the establishment of *Xylella Fastidiosa* in this region.

For *Xylella Fastidiosa* infecting olive trees in Salento, Italy, the initial genetic investigation of this alien parasite revealed the presence of a previously undescribed sequence type identified as ST53 code [16]. This sequence type was previously only known to be present in various areas of North, Central, and South America. ST53, identified in southern Apulia, Italy, appears to have been introduced relatively recently from Costa Rica [14,17]. Furthermore, it has been identified in other European regions, including France (Provence-Alpes-Côte d’Azur and Corsica), Spain (Balearic Islands and Madrid), and Portugal (Porto metropolitan area) [18]. The ability to trace and understand the movement and impact of such parasites across different regions underscores the importance of comprehensive and collaborative research efforts.

As there is still no identified treatment enabling the recovery of infected trees, the primary strategy to contain the epidemic involves the removal of infected trees. Thus, minimizing the risk of infection spread hinges on early identification, whether of asymptomatic trees or those displaying visible symptoms of desiccation. Detecting these trees early on is pivotal. Visual inspection remains the most widely used method due to its speed, simplicity, and cost-effectiveness. However, its accuracy relies heavily on the subjective assessment of disease severity. Moreover, a limitation arises from the fact that collected samples must undergo laboratory analysis. This turns visual inspection into a time-consuming, expensive, and intrusive detection method for *Xylella Fastidiosa* [19].

Earth observation (EO) technologies are widely acknowledged as potent instruments for the analysis, comprehension, and surveillance of Earth’s dynamic processes, spanning from a global to a local scale. The availability of long satellite time series has proven to be an invaluable resource, extensively utilized to discern regions undergoing deforestation or reforestation (<https://www.globalforestwatch.org/>) on a global scale down to a landscape level. Furthermore, appropriately processed and analyzed satellite time series empower us to glean insights into vegetation health, identifying areas susceptible to degradation or destruction. Satellite imagery is instrumental in monitoring the spread of invasive species, aiding in pinpointing regions where containment efforts are feasible. Additionally, this technology facilitates the detection and monitoring of plant diseases, thereby mitigating the likelihood of outbreaks and disease spread [20].

Notwithstanding the widely acknowledged potential of Earth observation (EO) technologies in general and satellite time series in particular, a significant and persistent challenge remains—the disconnect between the vast amount of available data and effective methodologies for extracting valuable information to enhance knowledge and facilitate long-term site monitoring. A primary hurdle lies in the fact that typical time series, such as those related to vegetation indices, inherently comprise three overlapping components: (i) seasonality (periodic behavior linked to plant phenology, driven by cover types, and modulated by weather artifacts such as temperature, rainfall, etc.); (ii) long-term trends, that is, gradual changes such as, for example, those linked to land degradation induced by

inter-annual climate variability (e.g. trends in mean annual rainfall, plant disease, parasite attacks, or change in land management, etc.), and (iii) residuals coupled with noise and linked, for example, to atmospheric scatter and cloud effects.

Over the years, various approaches have been developed to disentangle and quantify these overlapping components, each offering unique insights that may be of interest depending on the specific research focus [21].

In the characterization of forest disturbances, all of the diverse components (seasonal, abrupt, and gradual) may be of high interest because, according to the drivers [22], the disturbance may induce both variation in the “normal” seasonality and phenology as well as anomalous trends.

The case of alien parasites like *Xylella Fastidiosa* is paradigmatic, since the specific characteristics, behavior, and potential impact on vegetation, as well as the extent of induced damage, may be unknown due to their ability to adapt their biology and effects to specific ecosystems, vegetation species, and climatic conditions. For such cases, a timely and systematically updated characterization of the parasite’s impact on vegetation is crucial for effectively countering its diffusion.

In Italy, *Xylella Fastidiosa* was initially detected in an area encompassing approximately 8000 ha in the province of Lecce. It rapidly disseminated to most of the Apulian provinces, including Bari, Barletta, Andria, and Trani, posing a threat to an expansive surface area of about 750 thousand ha. This region accounts for nearly a third of the national olive production. *Xylella Fastidiosa* induces a swift decline in olive orchards, manifesting as leaf scorching and desiccation of twigs and branches, typically occurring at the uppermost part of the canopy. This progression can extend to the death of the tree, particularly affecting the most ancient century-old trees of the Cellina di Nardo and Ogliastro Salentina cultivars, which are among the most severely impacted varieties.

To counteract the diffusion of the parasite, it is imperative to thoroughly characterize its biology, potential variations, as well as its manifestations and effects on vegetation. This necessitates a comprehensive approach that combines in situ analyses with routinely conducted large-scale investigations, such as those facilitated by Earth observation (EO) technologies.

In contributing to this endeavor, our paper focuses on analyzing satellite MODIS-based evapotranspiration time series. This analysis spans both *Xylella Fastidiosa*-infected and -uninfected olive trees in Apulia and Basilicata. The aim is to assess and characterize the impact of *Xylella Fastidiosa* on the inner behavior of olive trees. The significance of this objective lies in the timely acquisition of baseline information crucial for understanding the disturbance caused by the parasite to olive tree change and dynamics. Such information is vital for supporting the formulation of effective attack strategies. Importantly, the proposed approach is versatile and can be promptly applied to detect vegetation disturbances and diseases induced by any parasite or degradation phenomenon.

2. Data and Study Area

The primary visible indication of infection by *Xylella Fastidiosa* in olive trees is the rapid desiccation of branches [17]. To identify these signs of disease presence, we carried out an analysis using moderate resolution imaging spectroradiometer (MODIS) evapotranspiration (ET hereafter) data. These data have the capability to monitor the water status of plants, allowing us to detect such disease-related symptoms. The data have a spatial resolution of 500 m and an 8-day sampling rate. They are freely available online (<https://lpdaac.usgs.gov>) and in the Google Earth Engine (GEE) cloud database.

The ET is calculated by summing up soil evaporation (E_s), canopy evaporation (E_c), and canopy transpiration (T_c):

$$ET = E_s + E_c + T_c \quad (1)$$

with

$$E_s = f_w \frac{\Delta A_s + \frac{(1-f_c)\rho_a C_p (e_s - e_a)}{r_a^s}}{\Delta + \gamma \frac{r_s^s}{r_a^s}} + RH \frac{(e_s - e_a)}{\beta_{sm}} (1 - f_w) \frac{\Delta A_s + \frac{(1-f_c)\rho_a C_p (e_s - e_a)}{r_a^s}}{\Delta + \gamma \frac{r_s^s}{r_a^s}} \quad (2)$$

$$E_c = f_w \frac{\Delta A_s + \frac{f_c \rho_a C_p (e_s - e_a)}{r_a^{wc}}}{\Delta + \gamma \frac{r_s^{wc}}{r_a^{wc}}} \quad (3)$$

$$T_c = (1 - f_w) \frac{\Delta A_c + \frac{f_c \rho_a C_p (e_s - e_a)}{r_a^t}}{\Delta + \gamma (1 + \frac{r_s^t}{r_a^t})}. \quad (4)$$

where f_c is the canopy cover, f_w is the pixel wet surface fraction, RH is the relative humidity, Δ is the gradient of the saturation vapor pressure—temperature, A_s and A_c are the available energy to the soil and canopy, respectively, γ is the psychrometric constant, β_{sm} is a parameter related to the soil moisture constraint, r_s^s and r_a^s are the surface and aerodynamic resistance for the soil surface, r_s^{wc} and r_a^{wc} are the surface and aerodynamic resistance for the wet canopy evaporation, and r_s^t and r_a^t are the surface and aerodynamic resistance for the canopy transpiration [23].

For our research aimed at identifying patterns associated with *Xylella Fastidiosa* in statistical features of evapotranspiration data, we carefully selected both infected and uninfected areas along with their respective MODIS pixels. Specifically, we pinpointed the infected areas based on in situ analysis and official online sources, dating back to October 2013, when Italian authorities notified the Commission of the initial outbreak of *Xylella Fastidiosa subspecies pauca* in southern Apulia, specifically in the Province of Lecce. Furthermore, the Apulia Region made reports, maps, and scientific papers publicly accessible through dedicated websites. These resources are regularly updated to provide current information. Specifically, the infected areas examined in this paper are those identified through:

- (i) European reports, available online since 2013, where *Xylella Fastidiosa* is regularly addressed in discussions with relevant authorities from EU member countries. These discussions occur during the monthly meetings of the Standing Committee on Plants, Animals, Food and Feed, specifically within the plant health section [24];
- (ii) official data from the Apulia region, available online, based on surveillance activities [25,26];
- (iii) independent investigations, such as those conducted by the Joint Research Center [27];
- (iv) systematic field surveys conducted by the authors since 2018.

The uninfected areas were chosen from the Apulia and Basilicata regions, which are situated at a considerable distance from the infected areas. Such uninfected areas have undergone systematic field investigations conducted by the authors of this paper since 2007 and continue to be monitored.

To select the areas covered by olive trees, we used the Corine land cover map, which has a specific class for cultivated areas planted with olive trees [28]. For the purpose of our investigation, within the infected zone (see Figure 1), we only selected the MODIS pixels covering the most homogeneous areas planted with olive trees. However, according to the Corine land cover nomenclature guidelines, and therefore for both infected and uninfected areas, the class olive tree can also include a percentage of vines or fruit plants intermixed with olives, bare soil or herbaceous vegetation among olive trees, scattered patches of semi-natural vegetation (greenery), interspersed annual crops, and irrigation ponds. None of these vegetation typologies are affected by *Xylella Fastidiosa*; therefore, it is reasonable to assume that in the absence of land use and land cover changes (which are systematically

updated in the Corine land cover, as for example, in the case of fire), the main variations observed are likely due to ecosystem disturbances such as the impact of *Xylella Fastidiosa*.

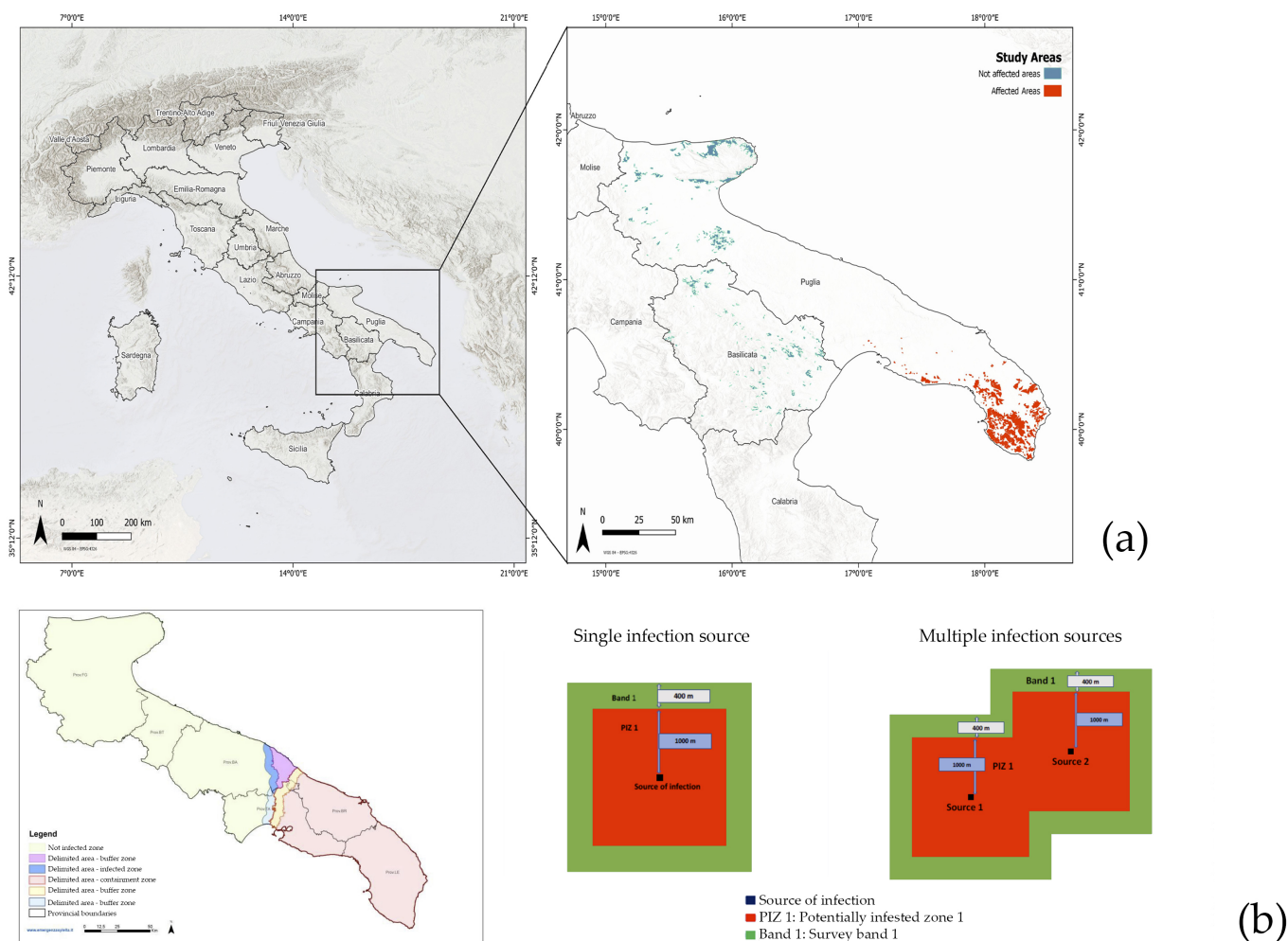


Figure 1. (a) Study area. (b) Left: areas (pink) marked as infected according to official data from the Apulia region. Right: the protocol implemented by the Apulia region for delineating infected areas involves the establishment of a 1 km boundary (illustrated by the red box of 1000 m) around the primary source of infection; additionally, a 400 m buffer zone (depicted by the green box of 400 m) is included when the source of infection has persisted in the investigated area for three years [29]. The image has been reworked by the authors.

The analysis of ET data encompasses the southeastern region of Italy, as depicted in Figure 1 that displays the areas identified as infected according to the official data updated as of December 2022 by the Apulia region [29]. The dataset spans from 2010 to 2022, and each pixel’s time series has a length of 575 samples, with missing data comprising less than 25%. Our investigation covers areas both infected and uninfected with *Xylella Fastidiosa*. In the infected region, we examined 989 pixels, while in the uninfected area, 1011 pixels were analyzed. It is worth noting that these two types of areas, the infected and the uninfected, are geographically distinct and do not overlap or adjoin one another. The selection of these areas was guided by their homogeneity in terms of topography and climate conditions. These regions exhibit relatively flat terrain, especially in the southeastern part of Apulia (where infected olive trees have been identified) and in the northeastern part of Apulia, as well as along the Ionian coast of Basilicata (where no evidence of *Xylella Fastidiosa* has been reported to date). In contrast, the northeastern part of Basilicata features hilly topographical

features and is characterized by a typical Mediterranean climate with cold winters and hot, dry summers.

We employed MODIS ET, as recommended by NASA, as a proxy indicator associated with vegetation water status, following the approach outlined in [30–32]. This choice was made due to the recognized utility of MODIS products in estimating ET, as indicated in [33].

3. Methods

3.1. The Singular Spectrum Analysis

There are several techniques for decomposing a time series into a certain number of independent components; among these, singular spectrum analysis (SSA) [34] represents an efficient and well-known decompositional method that is based on phase-lagged copies of the series. The independent components obtained by applying the SSA can be easily recognized as a slowly changing trend, oscillatory components, and structureless noise [35].

Let us consider a time series y_i ($i = 1, \dots, N$) and a lag M ; then, the Toeplitz lagged correlation matrix can be constructed:

$$c_{ij} = \frac{1}{N - |i - j|} \sum_{k=1}^{N - |i - j|} y_k y_{k + |i - j|}, \quad 1 \leq i, j \leq M \quad (5)$$

Sorting its eigenvalues λ_k in decreasing order, the corresponding eigenvectors E_{kj} where j and k vary from 1 to M are used to calculate the k -th principal component i , $0 \leq i \leq N - M$:

$$a_{ik} = \sum_{j=1}^M y_{i+j} E_{jk} \quad \text{for } 0 \leq i \leq N - M \quad (6)$$

and the k -th reconstructed component of the time series:

$$R_k = \frac{1}{M} \sum_{j=1}^M a_{i-j,k} E_{jk} \quad \text{for } M \leq i \leq N - M + 1 \quad (7)$$

Since the eigenvalue λ_k represents the fraction of the total variance of the original series explained in the k -th reconstructed component R_k , the decreasing order of the eigenvalues also reflects the decreasing order of the reconstructed components by the fraction of the total variance of the series [36]. SSA requires that the lag M is properly selected. Khan and Poskitt [37] calculated the maximum $M = (\log N)^c$, $1.5 \leq c \leq 2.5$.

3.2. The Fisher Information Measure and the Shannon Entropy

The Fisher–Shannon analysis relies on the computation of two informational quantities: the Fisher information measure (FIM) and Shannon entropy (SE). These metrics gauge the local and global characteristics, respectively, of the probability distribution function of the time series. FIM serves as an indicator of order and organization [38], whereas SE serves as an indicator of uncertainty or disorder in the series [39]. Their definitions are as follows:

$$FIM = \int_{-\infty}^{+\infty} \left(\frac{\partial}{\partial x} f(x) \right)^2 \frac{dx}{f(x)} \quad (8)$$

$$SE = \int_{-\infty}^{+\infty} f_X(x) \log(f_X(x)) dx \quad (9)$$

where $f(x)$ is the distribution of the series' values x . The Shannon entropy power N_X , which is always positive, is generally used instead of SE:

$$N_X = \frac{1}{2\pi e} e^{2SE}. \quad (10)$$

The Fisher information measure and N_X are interconnected through the isoperimetric inequality expressed as $FIM \cdot N_X \geq D$ [40], where D represents the dimension of the space (which is 1 for time series). In the so-called Fisher–Shannon Information plane (FSIP) the axes are FIM and N_X , and it can be employed to graphically represent time series data as points constrained to the domain $FIM \cdot N_X \geq 1$. Notably, the minimum value of $FIM \cdot N_X$ is 1, which occurs only for series with a Gaussian distribution. As a result, the FSIP, by combining the global and local characteristics of SE and FIM, offers a valuable approach to differentiate between various temporal dynamics within time series data [40].

3.3. The ROC Analysis

Receiver operating characteristics (ROC) analysis is employed to assess classifier performance. In binary classification scenarios, instances are categorized as either “positive” or “negative”, and a classifier assigns these instances to predicted classes.

When evaluating a classifier against an instance, four potential outcomes exist. The instance may be categorized as follows: true positive (TP) if it is positive and correctly classified as positive; false negative (FN) if it is positive but incorrectly classified as negative; true negative (TN) if it is negative and correctly classified as negative; or false positive (FP) if it is negative but inaccurately classified as positive [41]. We can define the following ratios: the *true positive rate* (TPr) and the *false positive rate* (FPr)

$$TPr = \frac{\text{Number of TP}}{\text{Total positives}} \quad (11)$$

$$FPr = \frac{\text{Number of FP}}{\text{Total negatives}} \quad (12)$$

An ROC curve is a graphical representation consisting of the TPr on the y-axis and the FPr on the x-axis. In ROC space, the point (0, 1) signifies perfect classification, and one point is considered better than another if it lies to the northwest of the first point. The diagonal line, represented by the equation $y = x$, corresponds to random classification, while an effective classifier is represented by a point located in the upper region of the ROC space.

Certain classifiers provide a score, which is a numeric value indicating the degree to which an instance belongs to a class. A scoring classifier can be used with a threshold to transform it into a binary classifier. Depending on the relationship between the output score and the threshold, the classifier assigns instances as positive or negative. Each threshold value generates a point in ROC space; by varying the threshold across a range of values, a curve can be traced through ROC space, and this curve is called the ROC curve. The area under the ROC curve (AUC) is commonly used to quantify the classifier’s performance.

Every point on the ROC curve represents a TPr/FPr trade-off associated with a specific threshold. Typically, to maximize this trade-off, the point on the ROC curve closest to (0, 1) is selected, and the corresponding threshold is used for classification.

4. Results

After normalizing the data (i.e., scaling to obtain a mean of 0 and a standard deviation of 1), we applied the Fisher–Shannon method to the time series of each pixel. Figure 2 displays the distributions of FIM and SEP for infected and uninfected sites, as well as FSIP, respectively. The distributions of FIM and SEP for the infected sites are both more peaked and narrower compared to those for the uninfected sites. On average, the FIM of the infected site’s ET time series is smaller, while the SEP is larger than that of the uninfected sites. Additionally, the distributions of FIM and SEP for the uninfected sites exhibit more skewness compared to those for the infected sites. When examining FSIP, it becomes evident that the ET time series of the uninfected sites deviate more significantly from Gaussianity in comparison to those of the infected sites.

We analyzed the receiver operating characteristic (ROC) curve for both FIM and SEP to assess their ability to discriminate between infected and non-infected sites. ROC curves are widely recognized for evaluating the performance of binary classifiers [41] based on the relationship between the true positive rate (TPR) and false positive rate (FPR).

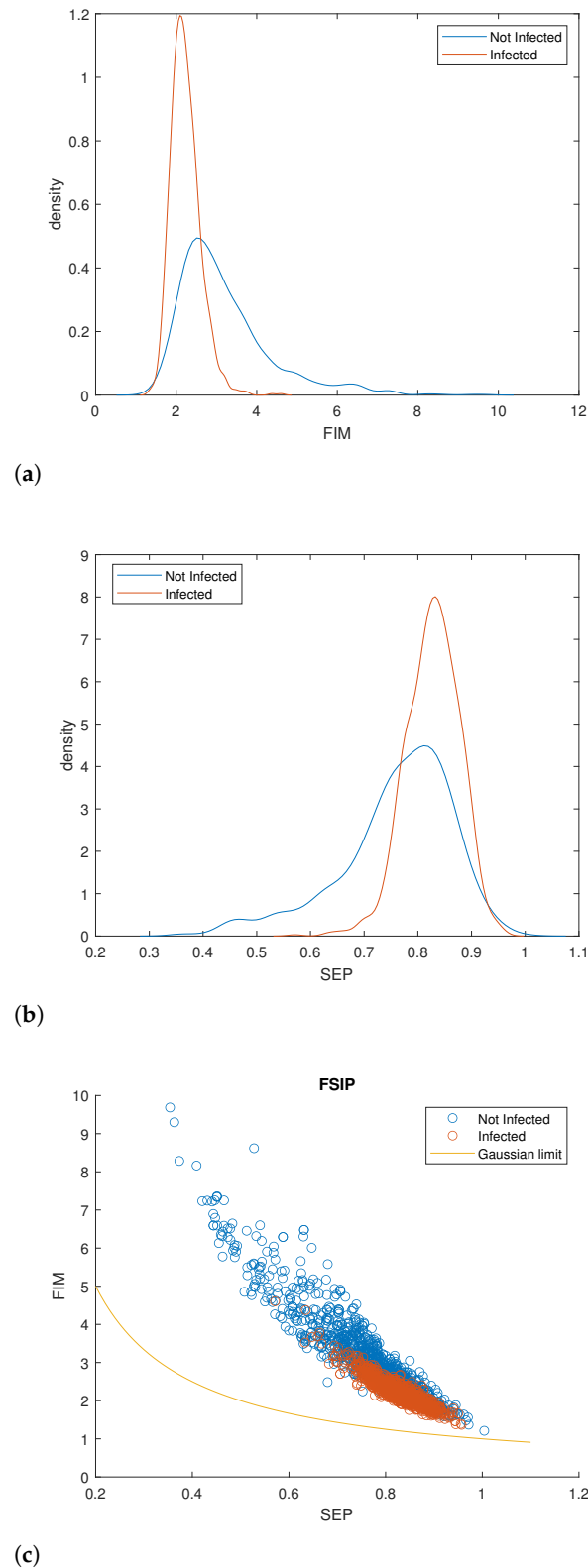


Figure 2. Distribution of FIM (a) and SEP (b) for infected and uninfected sites. (c) Fisher–Shannon information plane for infected and uninfected sites.

The construction of the ROC curve proceeds as follows: First, all the values of the chosen parameter (FIM or SEP) are arranged in ascending order. A threshold F is selected within the range of values, from the minimum to the maximum. Since the average value of SEP/FIM for the infected pixels is larger/smaller than that of the uninfected pixels, a TP is an SEP/FIM value from an infected pixel that is above/below F , while a FP is a SEP/FIM value from an uninfected pixel that is above/below F . An FN is an SEP/FIM value from an infected pixel that is below/above F , and a TN is an SEP/FIM value from an uninfected pixel that is below/above F . Thus, for each value of the threshold F within the range of minimum to maximum, the TPr and FPr can be calculated, yielding one point on the ROC curve. By varying the threshold value across the entire range and repeating this process, the complete ROC curve is generated. Following the construction of the ROC curve, the optimal threshold value corresponds to the point on the ROC curve closest to the coordinates (0, 1). Figure 3 displays the ROC curves for the FIM and SEP of the original ET time series. The optimal thresholds for FIM and SEP are found to be 2.45 and 0.81, respectively. Notably, the TPr for FIM is slightly higher than that for SEP, while the FPr is lower. The AUC for FIM is relatively high at 0.81, indicating better discriminatory performance compared to SEP, which has an AUC of 0.69.

The ET time series exhibit oscillating variability attributed to annual and six-month cycles, reflecting phenological vegetation cycles correlated with meteorological and climatic oscillations. To investigate the intrinsic temporal dynamics of vegetation that are not influenced by meteorological and climatic oscillations, we filtered out the annual and six-month cycles and analyzed the resulting residuals. To filter out these two cycles, we applied singular spectrum analysis to each pixel time series. SSA is well-suited to finding oscillatory components in short time series that are also affected by gaps, as is the case in our study.

The singular spectrum analysis requires that the lag M be properly selected. Due to the 8-day sampling time, we selected a lag of $M = 46$, which guarantees the detection of annual and sub-annual components; furthermore, this value fulfills Khan and Poskitt's criterion [37]. We applied SSA to each pixel time series for the infected and uninfected areas. Figure 4 illustrates, as an example, the steps of the SSA method applied to a pixel time series of the infected area. After normalizing the time series (Figure 4a), we calculated the eigenvalues (Figure 4b) that, when sorted in decreasing order, correspond to the components whose contribution to the total variance of the series decreases with the order of the eigenvalues. The major contribution to the variance of the series comes from the first four components; the first and second components represent the yearly cycle (Figure 4c), contributing to the total variance by about 24% each, while the third and fourth components represent the 6-month cycle (Figure 4d), contributing to the total variance by about 16% each. After removing the yearly cycle (subtracting the first and second components from the original normalized time series), we obtain the residual (Figure 4e), and after removing the third and fourth components as well, we get the residual (Figure 4f). We calculated the FIM and SEP for each residual time series (both those obtained after eliminating just the annual component and those obtained after also removing the 6-month components). Figure 5 shows the comparison between the FSIPs of the original and residual series. The informational pattern observed in the original data is also reflected in the residual data. The residual ET time series of the uninfected sites deviate significantly more from Gaussianity compared to those of the infected sites. Furthermore, there is a tendency for the SEP to decrease from the original case to that with the yearly component removed and further to that with the 6-month component also removed, while the FIM, on the contrary, tends to increase. Since the FIM can be considered as describing the "locality" of the distribution of the data, meaning that it quantifies its sensitivity to local fluctuations (while the SEP describes the "globality" of the distribution, quantifying its sensitivity to global variations), the obtained FSIP pattern could suggest that the distribution of the residual data is more sensitive to local variations, which are overwhelmed by the dominant annual and semi-annual cycles in the original data.

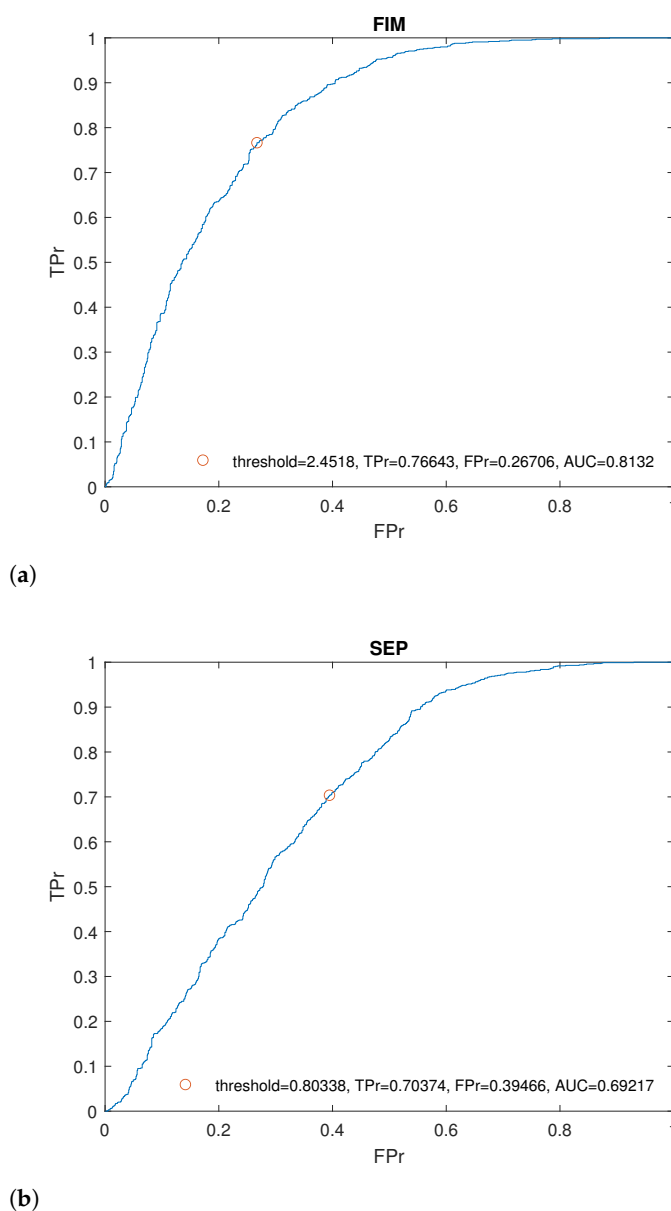


Figure 3. Receiving operating characteristic curve of FIM (a) and SEP (b) for the original data.

Figure 6 shows the distribution of FIM and SEP, along with their respective ROC curves, for the residual obtained after removing the annual cycle. Figure 7 shows the same for the residual obtained after removing both the annual and 6-month cycles. The values of the optimal threshold, TPr, FPr, and AUC are displayed in Tables 1 and 2. Comparing the results, we observe that the best performance among the two classifiers is achieved with the residuals obtained after removing just the annual cycle. For the FIM, using an optimal threshold of 2.96 yields the highest TPr (0.83), the lowest FPr (0.22), and the largest AUC (0.87). Regarding the SEP, while the TPr for the threshold 0.43 is not the highest (0.72 compared to 0.74 when both cycles are removed), it still yields the lowest FPr (0.16) and the largest AUC (0.86).

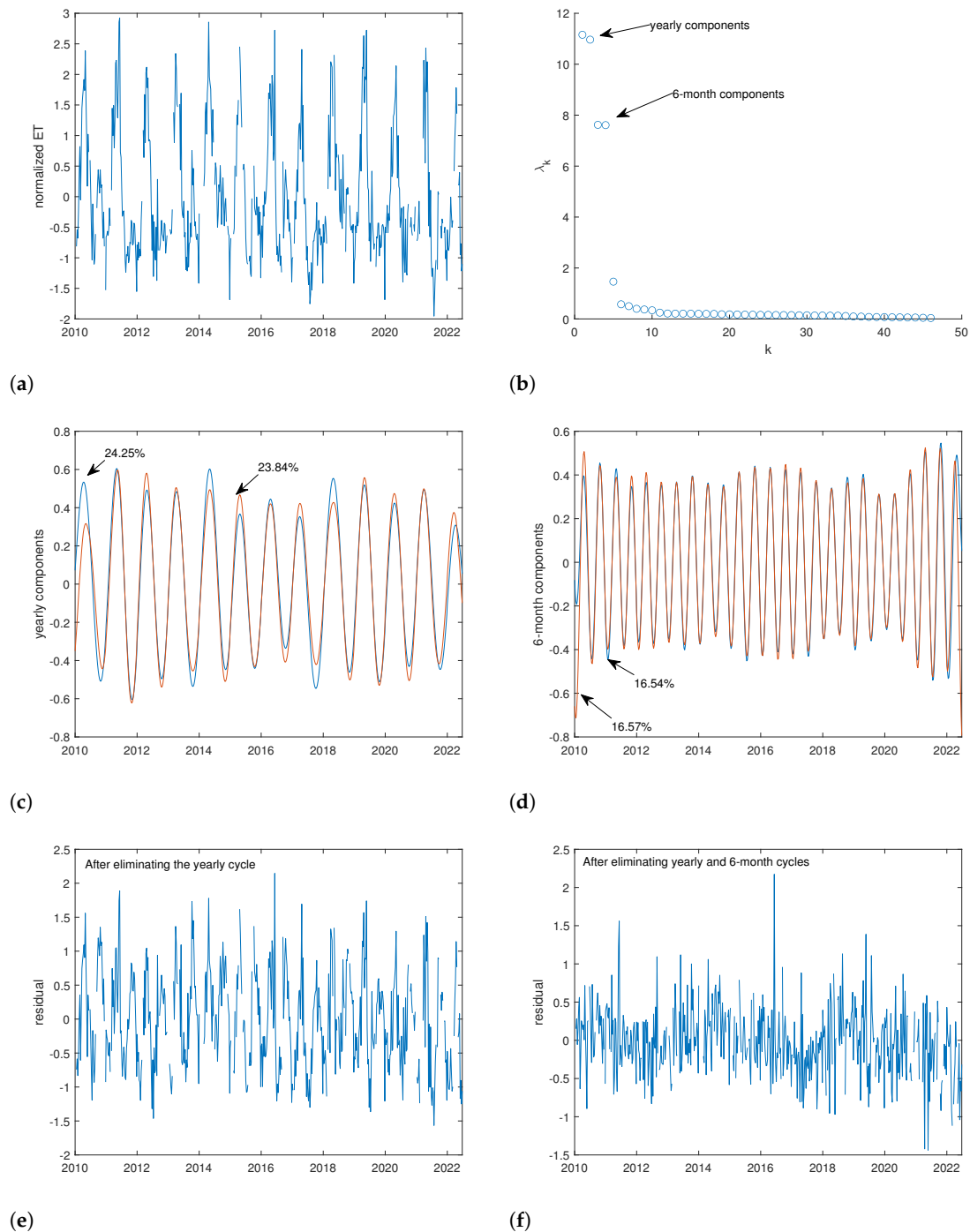


Figure 4. Steps of the SSA applied to a pixel time series for the infected area: (a) Normalized pixel time series. (b) Spectrum of the obtained eigenvalues; the first two eigenvalues correspond to the annual components (shown in (c)), while the third and fourth eigenvalues correspond to the 6-month components (shown in (d)). (e) Residual time series after removing the first two components corresponding to the annual cycle. (f) Residual time series after removing the first four components corresponding to the annual and 6-month cycles.

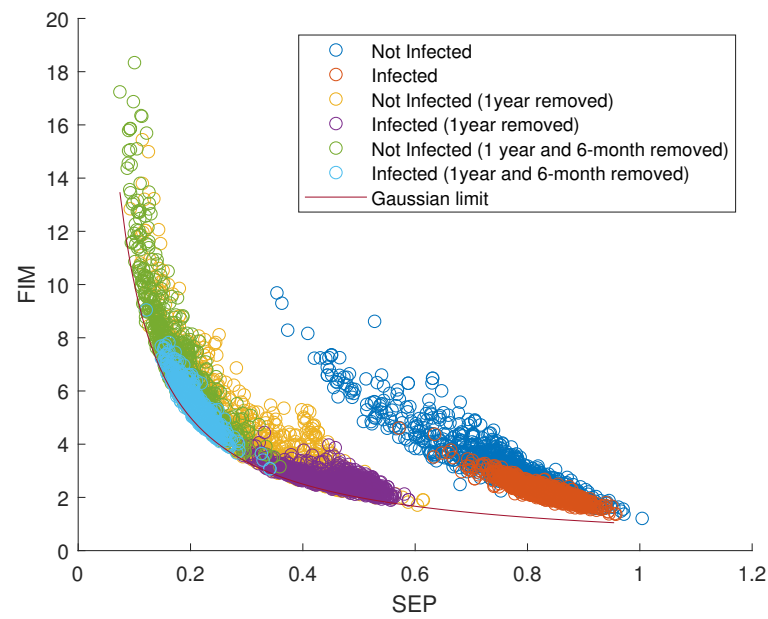


Figure 5. Fisher–Shannon information plane for infected and uninfected sites for the original and filtered data.

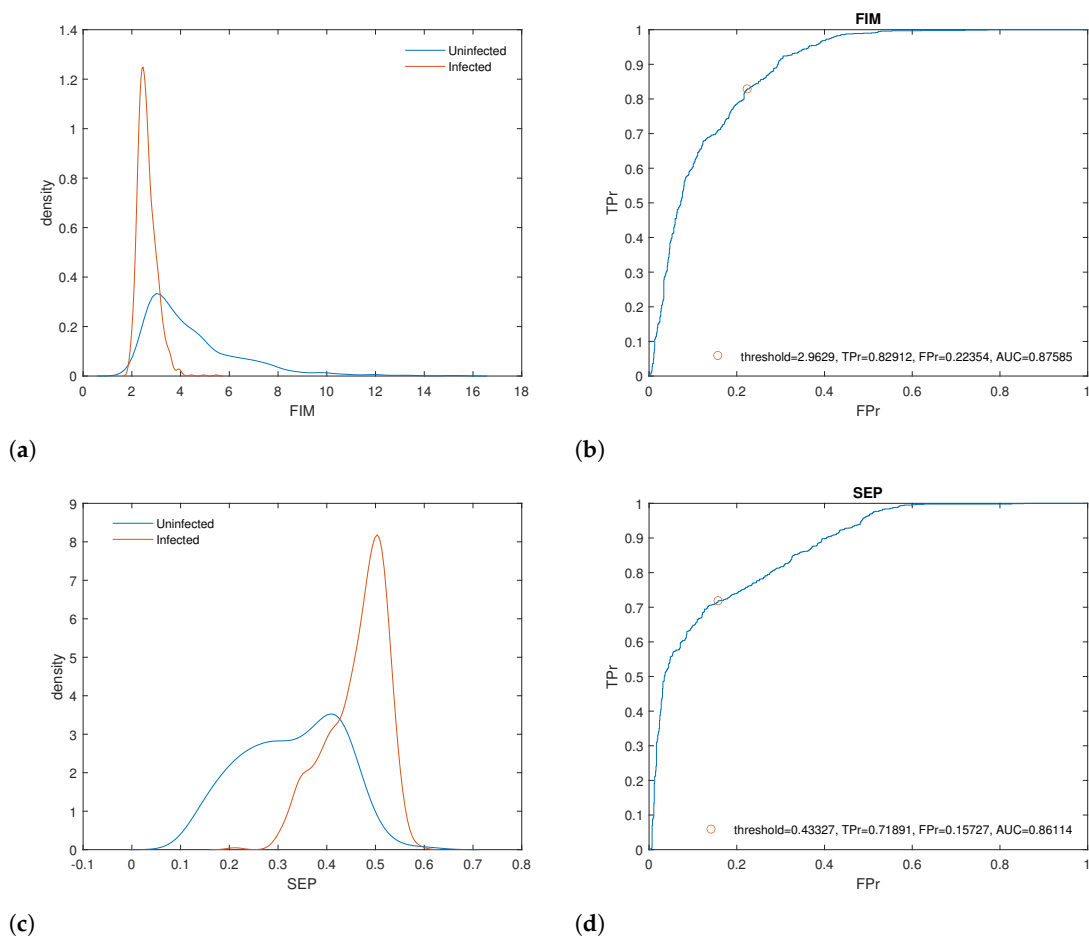
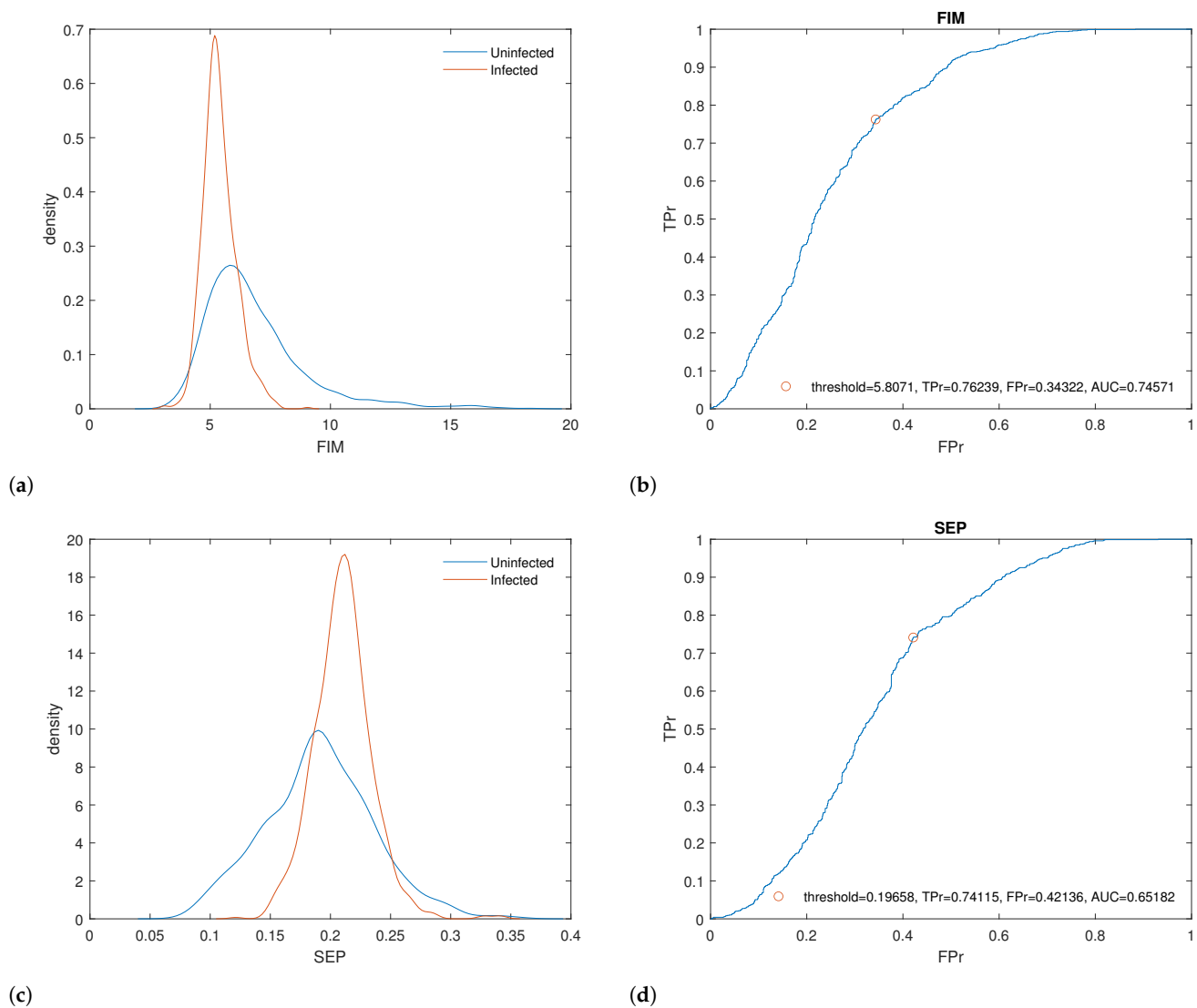


Figure 6. Distribution of FIM (a) and SEP (c) for infected and uninfected sites and (b,d) their receiving operating characteristic curves after filtering out the annual components.

Table 1. Results of the ROC analysis for FIM from each dataset. The AUC is the area under the ROC curve. The threshold, TPr, and FPr correspond to the point of the ROC curve closest to (0, 1).

Data	Threshold	TPr	FPr	AUC
Original	2.45	0.77	0.27	0.81
1-year component removed	2.96	0.83	0.22	0.87
1-year and 6-month components removed	5.81	0.76	0.34	0.74

**Figure 7.** Distribution of FIM (a) and SEP (c) for infected and uninfected sites and (b,d) their receiving operating characteristic curves after filtering out the annual and 6-month components.**Table 2.** Results of the ROC analysis for SEP of each dataset. The AUC is the area under the ROC curve. The threshold, TPr, and FPr correspond to the point of the ROC curve closest to (0, 1).

Data	Threshold	TPr	FPr	AUC
Original	0.80	0.70	0.39	0.69
1-year component removed	0.43	0.72	0.16	0.86
1-year and 6-month components removed	0.20	0.74	0.42	0.65

5. Discussion

The evapotranspiration process is influenced by several factors, including plant species, canopy characteristics, plant population, degree of surface cover, plant growth stage, irrigation management, soil physical, hydraulic and chemical characteristics, disease pressure, and geographic location including elevation, latitude, and longitude. Among all of the aforementioned factors, ET is primarily driven by climatic conditions and plants' conditions (plant health and soil–water status) and interactions with the climate [42]. The two main processes governing evapotranspiration are the soil evaporation and canopy transpiration, whose contribution to the evapotranspiration has been calculated with slightly different results depending on the type of crop vegetation, period of observation, etc. For instance, Wang et al. [43] for a maize crop found that soil water evaporation and crop transpiration had average values of 0.9 and 4.0 mm/d, respectively, with a relative dominance of the transpiration over the soil evaporation. López-Olivari et al. [44] evaluated the partitioning of actual evapotranspiration in soil evaporation and transpiration over a superintensive drip-irrigated olive orchard in Chile and found that ratios of transpiration and soil evaporation to actual evapotranspiration ranged between 0.64–0.74 and 0.26–0.36. Tezza et al. [45] measured and modelled soil evaporation in olive orchards in Portugal and found that, during a typical summer, the ratio between soil evaporation and canopy transpiration was 0.3 on average, and the ratio between soil evaporation and evapotranspiration ranged between 0.3 and 0.15. However, they also asserted that “the complexity of the canopy geometry with variable positional shadings along the days and seasons, overlapping with the individual geometry of the wet surfaces and variable turbulence, makes it very difficult to generalize models for evaporation below crowns”; in other words, the canopy plays an important role in the evapotranspiration process. In fact, Imark [42] highlighted that soil evaporation has a maximum during the early vegetation growing season and then gradually decreases as the leaf area increases, reaching the minimum when the canopy completely shades the soil surface; as the crop canopy develops and covers the soil surface, evaporation from the soil surface decreases and transpiration increases. In the cases examined in our study, the canopy of infected olive trees is almost absent since the effect of *Xylella* is to dry up the leaves of the tree. Therefore, this effect leads to lower evaporation and transpiration of the canopies of infected trees compared to those of the healthy ones and to relatively higher soil evaporation in the infected area compared to the healthy one.

Timely baseline information for comprehending the impact of parasite disturbances on olive tree change and dynamics is essential for supporting the formulation of effective strategies to address and combat such attacks. This is particularly relevant for *Xylella Fastidiosa*, as, since its initial identification in Apulia, it has infected approximately 4 million trees in the outbreak area [6]. The bacterium has resulted in, and continues to cause, substantial economic losses in terms of olive trees and oil production. It has also led to dramatic transformations in the Mediterranean landscape, where olive trees represent a deeply ingrained aspect of cultural heritage and a significant component of the flourishing tourism industry. Considering only the Apulia area, *Xylella Fastidiosa* could potentially inflict damages exceeding 5.2 billion euros over the next 50 years if the epidemic is not effectively managed with appropriate control measures and the replacement of infected plants [6]. The rapid spread of the pathogen and its evident high polyphagy suggest a concerning potential for extension into other regions across Europe and the Mediterranean. Additionally, there is the possibility of an expanded range of host species, leading to variations in the epidemiology and manifestations of its pathogenicity.

Thus, the characterization of the impact of this parasite on olive vegetation is extremely important in order to counteract its diffusion, and the MODIS ET data seems to enable us to better characterize and discriminate olive orchard areas infected by *Xylella Fastidiosa* from the uninfected ones.

The potential use of ET data for monitoring pest and parasite attacks at both landscape and field scales has been investigated by Telesca et al. [46,47], who showed the effectiveness of MODIS ET and other vegetation indices in assessing the deterioration of pine tree

vegetation caused by the parasite *Toumeyella Parvicornis*. Furthermore, the application of multifractal detrended fluctuation analysis at MODIS ET time series has suggested the employment of this satellite product as a good indicator of pathogenic status induced by *Xylella Fastidiosa* in olive trees [20,48].

According to Ciervo et al. [49], *Xylella Fastidiosa* is not the primary cause of the rapid desiccation of olive trees, since it damages plants that have already been weakened by environmental stressors such as reduced rainfall, excessive use of chemical herbicides, and soil organic matter depletion. These critical factors collectively favor those critical environmental conditions for the plants, diminishing their vigor and increasing vulnerability to parasites and infections, like those caused by *Xylella Fastidiosa*.

Certainly, the use of ET appears promising for characterizing and capturing the impact of *Xylella Fastidiosa* infection on plants. Given that one of the noticeable effects of this infection is the rapid desiccation and death of the plant, ET proves to be well-suited for providing insights into the water status of plants. It serves as an indirect measure of the loss of water content in vegetation. Therefore, considering that the primary symptom of *Xylella Fastidiosa*-induced disease is rapid desiccation, ET is a valuable tool for detecting the presence of this bacterium.

The application of the Fisher–Shannon method to pixels encompassing both healthy and *Xylella Fastidiosa*-infected olive groves in southern Italy has yielded insights into the temporal dynamics of ET data. On average, the ET time series of infected sites are characterized by a greater SEP and a lower FIM compared to those of healthy sites (Figure 8). Given that FIM and SEP relate to the local and global properties of the ET distribution, respectively, the larger SEP in infected sites suggests that global variations dominate their distribution. Conversely, the distribution of ET series for healthy sites is implied to be dominated by local variations. Figure 9 shows the distributions of the original normalized ET data for infected and uninfected pixels. The ET distributions of uninfected sites display a more prominent peaked behavior than those of infected sites, leading to a greater sensitivity to local variations in the ET distributions of non-infected pixels compared to the infected ones.

The observed disparity in informational response between the two types of sites may be linked to distinct nutritional processes, particularly the significant damage inflicted on the nutritional system in infected trees. The plant's nutritional system is based on mechanisms governing the flux of water and nutrients from the roots to the stem and leaves. Consequently, a healthy tree is characterized by a complex nutritional system that engages in dynamic interactions with the environment; therefore, a healthy tree would exhibit greater efficiency in reacting to local environmental factors. This heightened adaptability implies a higher resilience to external influences, resulting in increased heterogeneity, reflected in a larger FIM or a lower SEP (Figure 8).

The ROC analysis indicates the good performance of the two informational parameters (FIM and SEP) in distinguishing between healthy and *Xylella Fastidiosa*-infected sites (Figure 3). However, it suggests that FIM is more effective than SEP for detecting signs of *Xylella Fastidiosa* infection. The findings confirm and, in fact, enhance the outcomes observed in [20,48], where Fourier filtering of seasonal patterns was applied to the dataset.

In all of the examined sites, whether infected or uninfected, there is an observed cyclic component in the time variability of evapotranspiration (ET), and this is likely associated with meteorological and climatic seasonal cycles. Two distinct periodicities have been identified, specifically the annual and semi-annual cycles. Figure 10 shows the monthly means of the original ET series averaged over all the pixels for the uninfected and infected sites. The semi-annual periodicity is more pronounced in the infected pixels compared to the uninfected ones; in fact, the monthly means exhibit two distinct peaks in April and October. The heightened semi-annual pattern observed in infected sites is likely attributed to the varying vegetation status between uninfected and infected trees. A pixel covering an olive grove comprises not only olive trees but also background vegetation. Consequently, both olive trees and background vegetation contribute to the ET of a pixel. Until April/May,

the ET in both infected and uninfected olive groves rises in a similar manner, primarily due to the flowering of the background vegetation, which plays a predominant role in contributing to the overall ET. In summer, the background vegetation begins to dry, leading to a decrease in ET. However, this decline is more pronounced in infected sites. This is attributed to the lower contribution of olive canopies to the overall ET in infected sites compared to uninfected sites. Consequently, this disparity contributes to the emergence of a second peak in October, likely triggered by a re-flowering of background vegetation following rainfall. The distinct vegetational dynamics observed in infected and uninfected olive groves account for the enhanced FIM/SEP performance of ET in distinguishing between infected and uninfected trees after retaining the six-month cycle while eliminating only the annual cycle (see Tables 1 and 2).

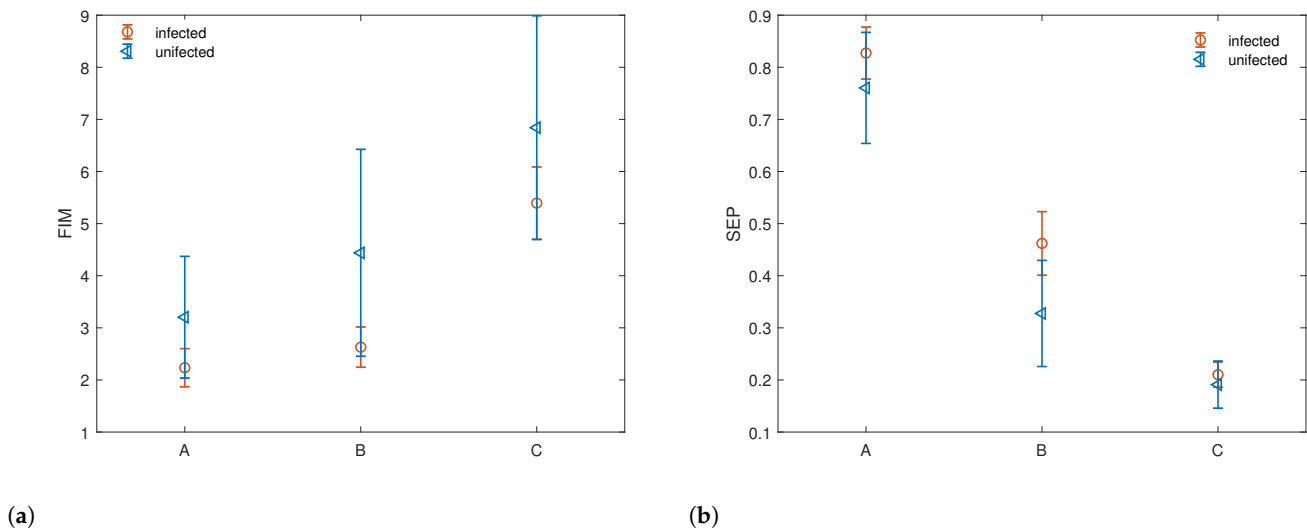


Figure 8. Averages of the FIM (a) and SEP (b) of the normalized ET for infected (blue) and uninfected (red) areas. The labels A, B, and C respectively indicate the original series, the series with the one-year cycle removed, and the series with both one-year and six-month cycles removed.

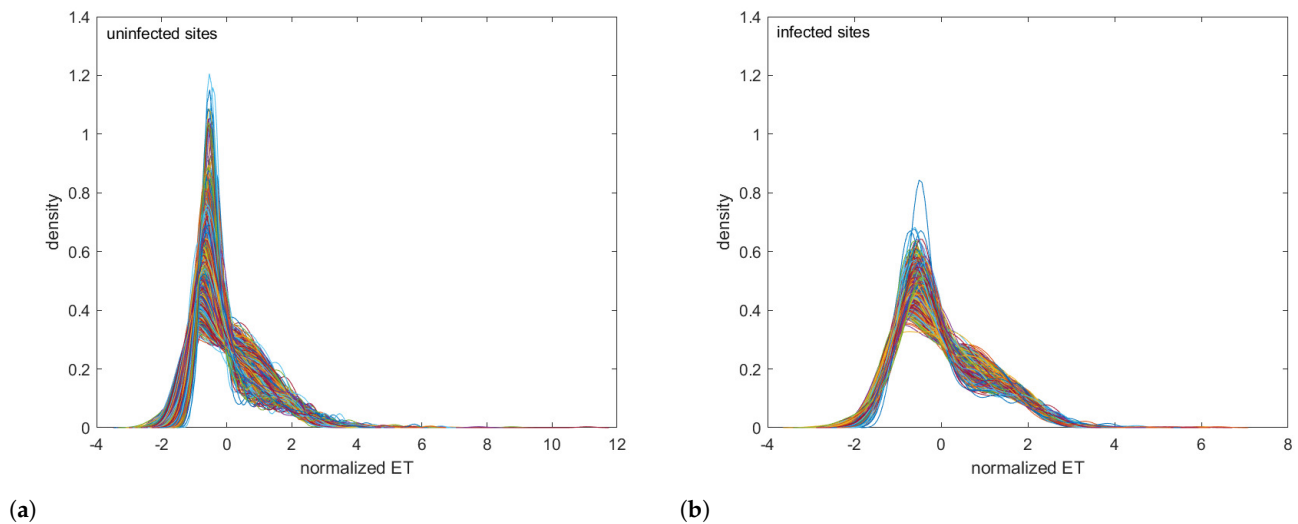
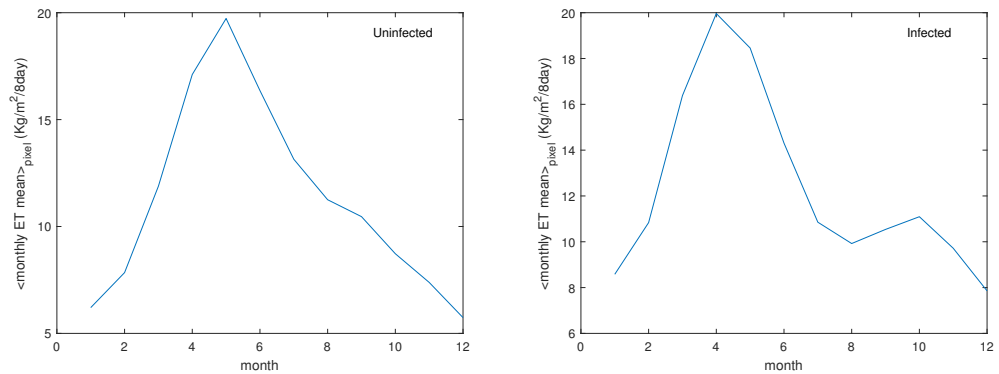


Figure 9. Distribution of normalized ET for uninfected (a) and infected (b) sites.



(a) (b)
Figure 10. Monthly ET means averaged over the analysed pixels for the uninfected (a) and infected (b) sites.

6. Conclusions

Our study aimed to distinguish between healthy and *Xylella Fastidiosa*-infected pixels covering olive groves in southern Italy using the Fisher–Shannon analysis, an informational method of analysis of time series. On average, the ET time series of *Xylella Fastidiosa*-infected sites exhibited a larger SEP compared to those of uninfected sites; conversely, the FIM was lower on average. This pattern is attributed to the distribution of ET values for both classes of pixels, with uninfected sites showing a more peaked distribution than infected ones. This behavior can be explained by the greater sensitivity of ET in uninfected sites to local distribution variations compared to that in infected sites.

The ROC analysis highlighted the good performance of the two informational parameters (FIM and SEP) in discerning between healthy and *Xylella Fastidiosa*-infected sites. Nonetheless, it indicated that FIM exhibits superior effectiveness compared to SEP in detecting symptoms of *Xylella Fastidiosa* infection.

As a concluding remark, our findings emphasize the importance of ET as a valuable indicator for diagnosing the extent of vegetation deterioration resulting from pest and parasite attacks. This underscores the critical role of ET as one of the most useful vegetation indices in assessing and monitoring the impact of such ecological challenges. Its importance has already been acknowledged across diverse fields, including climate change investigations, environmental monitoring, risk estimation, land management, agricultural practices, and food security. Consequently, these findings contribute to the development of operational tools for monitoring the biophysical parameters of vegetation status. This broader application reinforces the versatility and practical utility of ET in assessing and managing various aspects of ecological and agricultural systems.

Author Contributions: Conceptualization, L.T. and R.L.; methodology, L.T.; software, M.L.; formal analysis, L.T.; investigation, L.T. and R.L.; resources, R.L.; data curation, N.A.; writing—original draft preparation, L.T.; writing—review and editing, L.T. and R.L.; visualization, L.T.; project administration, R.L.; funding acquisition, R.L. All authors have read and agreed to the published version of the manuscript.

Funding: This research was supported by the project COELUM funded by the National Research Council of Italy.

Data Availability Statement: The raw data supporting the conclusions of this article will be made available by the authors on request.

Conflicts of Interest: The authors declare no conflicts of interest.

References

1. Pyšek, P.; Hulme, P.; Simberloff, D.; Bacher, S.; Blackburn, T.; Carlton, J.; Dawson, W.; Essl, F.; Foxcroft, L.; Genovesi, P.; et al. Scientists' warning on invasive alien species. *Biol. Rev.* **2020**, *95*, 1511–1534. [[CrossRef](#)] [[PubMed](#)]
2. Wallingford, P.; Morelli, T.; Allen, J.; Beaury, E.; Blumenthal, D.; Bradley, B.; Dukes, J.; Early, R.; Fusco, E.; Goldberg, D.; et al. Adjusting the lens of invasion biology to focus on the impacts of climate-driven range shifts. *Nat. Clim. Chang.* **2020**, *10*, 398–405. [[CrossRef](#)]
3. Chaloner, T.; Gurr, S.; Bebbler, D. Plant pathogen infection risk tracks global crop yields under climate change. *Nat. Clim. Chang.* **2021**, *11*, 710–715. [[CrossRef](#)]
4. Sorensen, J.; Gill, R. A range extension of *Homalodisca coagulata* (Say) (Hemiptera: Clypeorrhyncha: Cicadellidae) to southern California. *Pan-Pac. Entomol.* **1996**, *72*, 160–161.
5. Janse, J.; Obradovic, A. *Xylella Fastidiosa*: Its biology, diagnosis, control and risks. *J. Plant Pathol.* **2010**, *92*, S35–S48.
6. Schneider, K.; van der Werf, W.; Cendoya, M.; Mourits, M.; Navas-Cortés, J.; Vicent, A.; Oude Lansink, A. Impact of *Xylella Fastidiosa* subspecies pauca in European olives. *Proc. Natl. Acad. Sci. USA* **2020**, *117*, 9250–9259. [[CrossRef](#)] [[PubMed](#)]
7. Hearon, S.; Sherald, J.; Kostka, S. Association of xylem-limited bacteria with elm, sycamore, and oak leaf scorch. *Can. J. Bot.* **1980**, *58*, 1986–1993. [[CrossRef](#)]
8. Wells, J. Isolation, culture, and pathogenicity of the bacterium causing phony disease of peach. *Phytopathology* **1980**, *73*, 859. [[CrossRef](#)]
9. Saponari, M.; Boscia, D.; Nigro, F.; Martelli, G. Identification of DNA sequences related to *Xylella Fastidiosa* in oleander, almond and olive trees exhibiting leaf scorch symptoms in Apulia (Southern Italy). *J. Plant Pathol.* **2013**, *95*, 668.
10. Jeger, M.; Caffier, D.; Candresse, T.; Chatzivassiliou, E.; Dehnen-Schmutz, K.; Gilioli, G.; Grégoire, J.C.; Jaques Miret, J.; MacLeod, A.; Navajas Navarro, M.; et al. Scientific opinion on the updated pest categorisation of *Xylella Fastidiosa*. *EFSA J.* **2018**, *16*, 5357.
11. Krugner, R.; Sisterson, M.S.; Chen, J.; Stenger, D.C.; Johnson, M.W. Evaluation of olive as a host of *Xylella Fastidiosa* and associated sharpshooter vectors. *Plant Dis.* **2014**, *99*, 1186–1193. [[CrossRef](#)]
12. Haelterman, R.M.; Tolocka, P.A.; Roca, M.E.; Guzmán, F.A.; Fernández, F.D.; Otero, M.L. First presumed diagnosis of *Xylella Fastidiosa* causing olive scorch in Argentina. *J. Plant Pathol.* **2015**, *97*, 393.
13. Coletta-Filho, H.D.; Francisco, C.S.; Lopes, J.R.S.; De Oliveira, A.F.; Da Silva, L.F.O. First report of olive leaf scorch in Brazil, associated with *Xylella Fastidiosa* subsp. pauca. *Phytopathol. Mediterr.* **2016**, *55*, 130–135.
14. Giampetruzzi, A.; Chiumenti, M.; Saponari, M.; Donvito, G.; Italiano, A.; Loconsole, G.; Boscia, D.; Cariddi, C.; Martelli, G.P.; Saldarelli, P. Draft genome Sequence of *Xylella Fastidiosa* CoDiRO Strain. *Genome Announc.* **2015**, *3*, e01538-14.
15. Strona, G.; Carstens, C.J.; Beck, P.S.A. Network analysis reveals why *Xylella Fastidiosa* will persist in Europe. *Sci. Rep.* **2017**, *7*, 71. [[CrossRef](#)]
16. Elbeaino, T.; Yaseen, T.; Valentini, F.; Ben Moussa, I.E.; Mazzoni, V.; D'Onghia, A.M. Identification of three potential insect vectors of *Xylella Fastidiosa* in southern Italy. *Phytopathol. Mediterr.* **2014**, *53*, 328–332.
17. Saponari, M.; Giampetruzzi, A.; Loconsole, G.; Boscia, D.; Saldarelli, P. *Xylella Fastidiosa* in Olive in Apulia: Where We Stand. *Phytopathology* **2019**, *109*, 175–186. [[CrossRef](#)]
18. Morelli, M.; García-Madero, J.M.; Jos, A.; Saldarelli, P.; Dongiovanni, C.; Kovacova, M.; Saponari, M.; Baños Arjona, A.; Hackl, E.; Webb, S.; et al. *Xylella Fastidiosa* in Olive: A Review of Control Attempts and Current Management. *Microorganisms* **2021**, *9*, 1771. [[CrossRef](#)]
19. Bock, C.; Poole, G.; Parker, P.; Gottwald, T. Plant disease severity estimated visually, by digital photography and image analysis, and by hyperspectral imaging. *CRC Crit. Rev. Plant Sci.* **2010**, *29*, 59–107. [[CrossRef](#)]
20. Telesca, L.; Abate, N.; Faridani, F.; Lovallo, M.; Lasaponara, R. Discerning *Xylella Fastidiosa*-Infected Olive Orchards in the Time Series of MODIS Terra Satellite Evapotranspiration Data by Using the Fisher–Shannon Analysis and the Multifractal Detrended Fluctuation Analysis. *Fractal Fract.* **2023**, *7*, 466. [[CrossRef](#)]
21. Verbesselt, J.; Hyndman, R.; Newnham, G.; Culvenor, D. Detecting trend and seasonal changes in satellite image time series. *Remote Sens. Environ.* **2010**, *114*, 106–115. [[CrossRef](#)]
22. Senf, C.; Seidl, R.; Hostert, P. Remote sensing of forest insect disturbances: Current state and future directions. *Int. J. Appl. Earth Obs. Geoinf.* **2017**, *60*, 49–60. [[CrossRef](#)] [[PubMed](#)]
23. Laipelt, L.; Kayser, R.H.B.; Fleischmann, A.S.; Ruhoff, A.; Bastiaanssen, W.; Erickson, T.A.; Melton, F. Long-term monitoring of evapotranspiration using the SEBAL algorithm and Google Earth Engine cloud computing ISPRS. *J. Photogramm. Remote Sens.* **2021**, *178*, 81–96. [[CrossRef](#)]
24. Latest Developments on *Xylella Fastidiosa* in EU Territory. Available online: https://food.ec.europa.eu/plants/plant-health-and-biosecurity/legislation/control-measures/xylella-fastidiosa/latest-developments-xylella-fastidiosa-eu-territory_en (accessed on 25 November 2023).
25. Emergenza *Xylella*. Available online: http://www.emergenzaxylella.it/portal/portale_gestione_agricoltura/Cartografie (accessed on 25 November 2023).
26. Servizio di Informazione Territoriale della Regione Puglia. Available online: <http://webapps.sit.puglia.it/arcgis/services/Operationali/DatiPubbliciFasceXF/MapServer/WMServer> (accessed on 27 November 2023).
27. Monitoring Impacts of *Xylella Fastidiosa*. Available online: https://joint-research-centre.ec.europa.eu/jrc-news-and-updates/monitoring-impacts-xylella-fastidiosa-2019-11-12_en (accessed on 27 November 2023).

28. Corine Land Cover Nomenclature Guidelines.
29. Bollettino Ufficiale della Regione Puglia—n. 139 del 27-12-2022. 2022.
30. NASA Land Processes Distributed Active Archive Center (LP DAAC). Available online: <https://modis-land.gsfc.nasa.gov/ET.html> (accessed on 25 November 2023).
31. MOD16A2 MODIS/Terra Net Evapotranspiration 8-Day L4 Global 500m SIN Grid V006. Available online: <https://ladsweb.modaps.eosdis.nasa.gov/missions-and-measurements/products/MOD16A2> (accessed on 1 December 2023).
32. de Queiroga Miranda, R.; Galvncio Domiciano, J.; Beserra de Moura, M.S.; Jones, C.A.; Srinivasan, R. Reliability of MODIS Evapotranspiration Products for Heterogeneous Dry Forest: A Study Case of Caatinga. *Adv. Meteorol.* **2017**, *2017*, 9314801. [[CrossRef](#)]
33. Proceedings of the 26th Annual Symposium of the European Association of Remote Sensing Laboratories. Available online: <https://www.earsel.org/symposia/2006-symposium-Warsaw/pdf/260.pdf> (accessed on 25 November 2023).
34. Vautard, R.; Ghil, M. Singular spectrum analysis in nonlinear dynamics, with applications to paleoclimatic time series. *Phys. D* **1989**, *35*, 395–424. [[CrossRef](#)]
35. Hassani, H. Singular Spectrum Analysis: Methodology and Comparison. *J. Data Sci.* **2007**, *5*, 239–257. [[CrossRef](#)]
36. Schoellhamer, D. Singular spectrum analysis for time series with missing data. *Geophys. Res. Lett.* **2001**, *28*, 3187–3190. [[CrossRef](#)]
37. Khan, M.; Poskitt, D.S. Description Length Based Signal Detection in singular Spectrum Analysis. In *Monash Econometrics and Business Statistics Working Papers 13/10*; Monash University, Department of Econometrics and Business Statistics: Melbourne, Australia, 2010.
38. Frieden, B.R. Fisher information, disorder, and the equilibrium distributions of physics. *Phys. Rev. A* **1990**, *41*, 4265–4276. [[CrossRef](#)] [[PubMed](#)]
39. Shannon, C.E. A mathematical theory of communication. *Bell Syst. Tech. J.* **1948**, *27*, 379–423. [[CrossRef](#)]
40. Martin, M.; Perez, J.; Plastino, A. Fisher information and nonlinear dynamics. *Phys. A* **2001**, *291*, 523–532. [[CrossRef](#)]
41. Fawcett, T. An introduction to ROC analysis. *Pattern Recognit. Lett.* **2006**, *27*, 861–874. [[CrossRef](#)]
42. Irmak, S. Evapotranspiration Basics and Estimating Actual Crop Evapotranspiration from Reference Evapotranspiration and Crop-Specific Coefficients. 2017. Available online: <https://extensionpubs.unl.edu/publication/g1994/pdf/view/g1994-2017.pdf> (accessed on 5 December 2023).
43. Wang, Y.; Horton, R.; Xue, X.; Ren, T. Partitioning evapotranspiration by measuring soil water evaporation with heat-pulse sensors and plant transpiration with sap flow gauges. *Agric. Water Manag.* **2021**, *252*, 106883. [[CrossRef](#)]
44. Lopez-Olivari, R.; Ortega-Farıas, S.; Poblete-Echeverrıa, C. Partitioning of net radiation and evapotranspiration over a superintensive drip-irrigated olive orchard. *Irrig. Sci.* **2016**, *34*, 17–31. [[CrossRef](#)]
45. Tezza, L.; Hausler, M.; Conceicao, N.; Ferreira, M.I. Measuring and Modelling Soil Evaporation in an Irrigated Olive Orchard to Improve Water Management. *Water* **2019**, *11*, 2529. [[CrossRef](#)]
46. Telesca, L.; Aromando, A.; Faridani, F.; Lovallo, M.; Cardettini, G.; Abate, N.; Papitto, G.; Lasaponara, R. Exploring Long-Term Anomalies in the Vegetation Cover of Peri-Urban Parks Using the Fisher-Shannon Method. *Entropy* **2022**, *24*, 1784. [[CrossRef](#)] [[PubMed](#)]
47. Telesca, L.; Lovallo, M.; Cardettini, G.; Aromando, A.; Abate, N.; Proto, M.; Loperte, A.; Masini, N.; Lasaponara, R. Urban and Peri-Urban Vegetation Monitoring Using Satellite MODIS NDVI Time Series, Singular Spectrum Analysis, and Fisher–Shannon Statistical Method. *Sustainability* **2023**, *15*, 11039. [[CrossRef](#)]
48. Telesca, L.; Abate, N.; Faridani, F.; Lovallo, M.; Lasaponara, R. Revealing Traits of Phytopathogenic Status Induced by *Xylella Fastidiosa* in Olive Trees by Analyzing Multifractal and Informational Patterns of MODIS Satellite Evapotranspiration Data. *Phys. A* **2023**, *629*, 129163. [[CrossRef](#)]
49. Ciervo, M. The olive quick decline syndrome (OQDS) diffusion in Apulia Region: An apparent contradiction according to the agricultural model. *Rev. Belg. Geographie* **2016**, *4*, 1–22. [[CrossRef](#)]

Disclaimer/Publisher’s Note: The statements, opinions and data contained in all publications are solely those of the individual author(s) and contributor(s) and not of MDPI and/or the editor(s). MDPI and/or the editor(s) disclaim responsibility for any injury to people or property resulting from any ideas, methods, instructions or products referred to in the content.